ISTITUTO NAZIONALE DI FISICA NUCLEARE

Sezione di Milano

INFN/BE-05/02
October 10, 2005

AN OPTICAL SYSTEM DEVELOPED FOR TARGET LASER PULSE GENERATION

Simone Cialdi, Ilario Boscolo, Andrea Paleari

INFN, Sez. Milano and Dip. Fisica, Univ. Milano, 20133 Milano, Italy

Abstract

We present the optical system developed for laser pulse shaping investigations. The items of the system are: a mode-locked 5 W 100 MHz 90 ps Nd:YAG laser coupled to an optical fiber, a programmable pulse shaping system, an autocorrelator and a spectrometer. The system can be programmed to generate any target waveform compatible with the spectral bandwidth of the laser system. The generation of a 2 ps compressed pulse and of rectangular, double-pulse and multi-pulse profiles with fairly good stability is discussed. The system is built for tests of shaping systems arranged in different configurations.

PACS: 42.65.Ky, 07.05.Tp
Keywords: Nd:YAG, laser, optical fiber, shaping system, adaptive genetic algorithm, autocorrelator.

Published by ***SIS–Pubblicazioni***
Laboratori Nazionali di Frascati

1 Introduction

High brilliance radiofrequency electron guns (rf-gun) are driven by UV laser pulses [1–3]. Experimental tests reported in Ref. [4] showed that the e-beam emittance depends on the temporal laser pulse characteristics and the emittance reached a minimum with a rectangular pulse. A subpicosecond Gaussian-like laser pulse is transformed into a rectangular one by a shaping system properly arranged. A typical laser system incorporating a shaper is shown in Fig. 1.

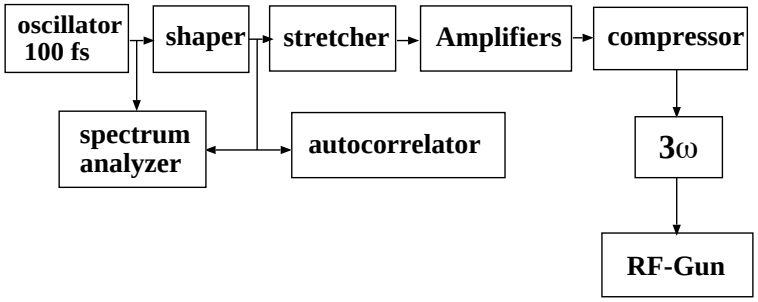

Figure 1: System layout with a pulse shaper insertion.

The technology for manipulating sub-picosecond pulses in order to generate ultrashort pulses according to user specifications has already been developed [5,6]. We apply the basic ideas developed for narrowing laser pulses (from picosecond to femtosecond range) for generating relatively long (around 10 picosecond) rectangular pulses with fast rise time (less than one picosecond). The principle of pulse shaping is based on the phase and amplitude modulation of the pulse spectral components. A rectangular pulse with a subpicosecond rise time can be obtained from a femtosecond laser pulse thanks to its high frequency content. However, the basic physics and properties of a shaping system capable of providing 10 ps rectangular pulses can be tested with a picosecond laser pulse, that is with a laser of the previous generation, therefore, not so much expensive. In the framework of developing shaping techniques for relatively long waveforms, we have designed and developed an actively mode-locked Nd:YAG delivering pulses of 90 ps at 100 MHz with an average power of 5 W, followed by a $500\ m$ monomodal optical fiber for broadening the spectral bandwidth of a factor higher than 100, passing from 0.02 to 2 nm. We have also developed the diagnostic tools, that is an autocorrelator and a spectrometer, for on-line pulse profile and spectrum measurements. The liquid crystal programmable spatial light modulator(LCP-SLM) shaper (also called 4f-system) [5] was selected for its capability to provide long laser pulses. It was configurated for phase modulation of the spectral components. This shaper and the diagnostic tools are connected to a computer in

a feed-back loop for autoconsistent operations. This system configuration is compulsory because the powerful lasers used to drive rf-guns (most commonly, Ti:Sa lasers operating at the third harmonic [1,2]) are multi-component systems (with amplifiers and harmonic converters) having inherent configurational perturbations and therefore some instability in the output waveform. This instability connected to the shaper sensitivity to it leads quite naturally to set the entire laser system in a self-organized mode of operation towards the generation of a target output pulse as we have developed, see Fig. 2 . We have designed and tested the system for the generation of pulses of rectangular, double-pulse and multi-pulse profiles. The several components and their behavior are presented and discussed in the following sections.

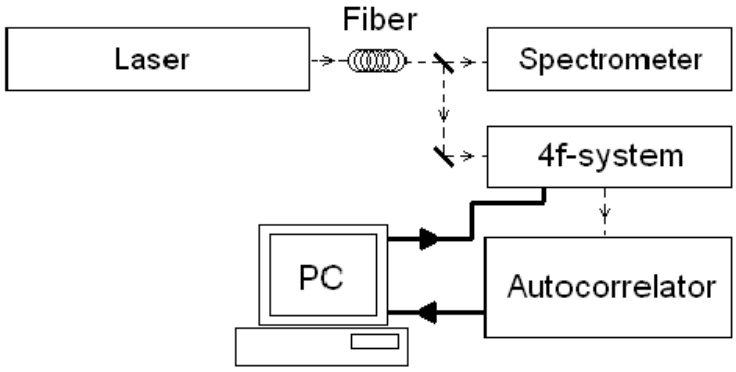

Figure 2: Schematic of the laser system complete of shaping system and the fundamental diagnostics.

2 The Nd:YAG oscillator

The Nd:YAG oscillator has been designed for actively mode-locked operation at 100 MHz and single TEM_{00} transverse mode. The laser medium (laser rod) is a 7 mm long and 2 mm diameter rod, side diode pumped (CEO diode pump model RB20-1C2). The two rod surfaces are tilted of 2 degrees with respect to the axis for avoiding etalon effect (the output pulse was instable and long with flat/flat surfaces). The acousto-optic-modulator AOM (IntraAction model ML-503B1) is driven by a 25 W RF-generator composed of an RF-synthetizer (Rohde&Schwarz) followed by an amplifier (LZY-1 of Mini-Circuit). The resonant frequency is 50,24106 MHz with an out-of-tuning tolerance less than 50 Hz. Only 5 W power was necessary for driving the AOM with a modulation amplitude of the laser power estimated around 50 %, when the frequency matching between the modulator and the RF-generator was set (reflected power was detected by a Rosmeter). The AOM temperature is fixed at 20 ^oC by water cooling so to have a stable operation.

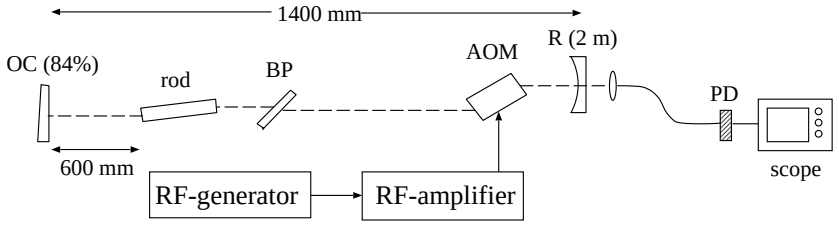

Figure 3: Schematic of Nd:YAG oscillator with its components: OC = Output Coupler, RM = Rear Mirror, BP = Beam Splitter, FD = photodiode

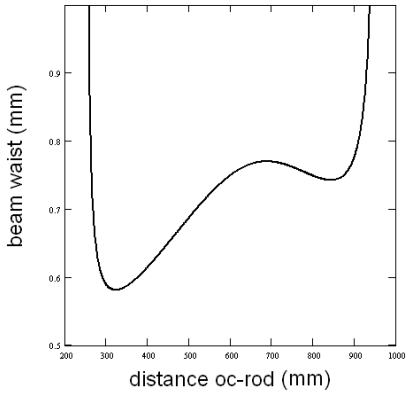

Figure 4: Dimension of the beam waist as function of the laser rod output coupler.

The design of the cavity was done exploiting the matrix propagation of the light beam through the optical components. The constrains of 100 MHz frequency, fundamental TEM_{00} mode and an optimized trade-off between the output power and the pulse length guided the choices (shown in Fig. 3) of cavity length, laser rod position, radius of the rear reflector mirror and transmittance of the flat output coupler. The TEM_{00} and the maximum output power result from the precise ratio between the diameters of the beam waist and of the back of the rod surface (where the beam waist is programmed by the cavity project). A too-large beam waist leads to un-wanted losses, a too-small beam waist leads to the presence of un-wanted higher modes (which, by the way, perturbs the mode-locking operation). Technically, the right matching is reached moving slightly the laser rod while looking at the output power (in a power meter) and the mode configuration (in a phosphor screen, but also through the beating frequency in an electronic spectrometer). The variation of the beam waist as function of the output coupler-laser rod distance (at the rod external surface) is depicted in Fig. 4. The cavity design meets the stability condition for the laser rod positioned at 250-950 mm interval from the output coupler. In particular, the position optimized for TEM_{00} mode, highest power level and good stability was found to be around 600 mm.

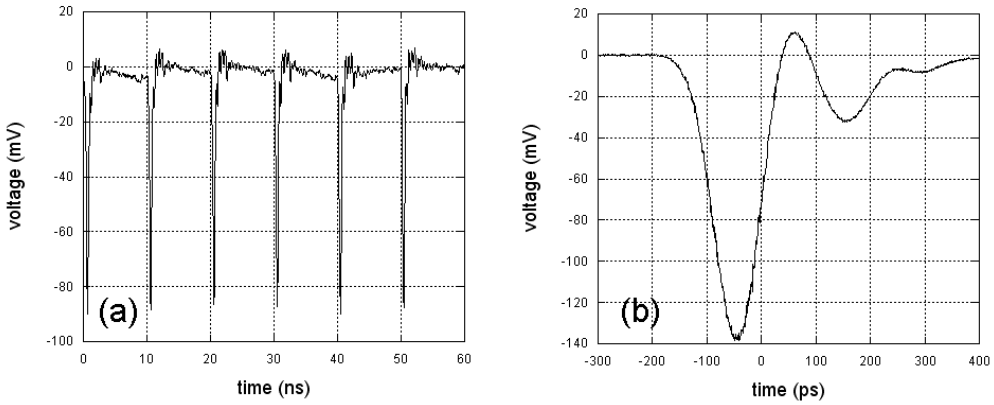

Figure 5: Output pulses: Frame a shows the train of pulses a good stability; Frame b shows the single pulse width (the overshoot at the end of the pulse is due to the pic-up monitor.

Fig. 5 shows the train and the single pulse shape detected by a 30 ps rise-time photodiode (Martin Froeschner & Associates) placed at the rear mirror and recordered by a 2 GHz LeCroy scope and 12.5 GHz Tektronix sampling respectively. The high responsivity of the photodiode, 0.9 A/W at 1550 nm could catch the light leak from the 99.9 reflectivity rear mirror. The depicted pulse has a length of 93 ps. The standard deviation measured by the sampling scope was 1.5 ps. That pulse train had an average power of 1.5 W with 20.5 A current feeding the diodes (the laser rod was not operating at the best because of thousands hours of operation).

The best observed result was 70 ps. This was obtained with fine tuning of AOM configuration (alignment along the three axis es, RF-tuning and high modulation), fine tuning of the cavity length (the output mirror is submicrometrically set) and fine alignment of the laser rod.

3 Bandwidth broadening by a 500 m optical fiber insertion

A guided optical wave propagating in a single mode fiber experiences a uniform self-phase modulation which broadens the spectrum. We have coupled the Nd:YAG laser to a 500 m long single mode, polarization preserving optical fiber for extending the spectrum of our laser pulse from the initial 0.02 to a final 2 nm, see Fig. 6. In fact, in the propagation equation

$$\frac{\partial^2 \vec{E}}{\partial z^2} - \frac{\epsilon_r}{c^2}\frac{\partial^2 \vec{E}}{\partial t^2} = \mu_0 \frac{\partial^2 \vec{P}_{NL}}{\partial t^2} \tag{1}$$

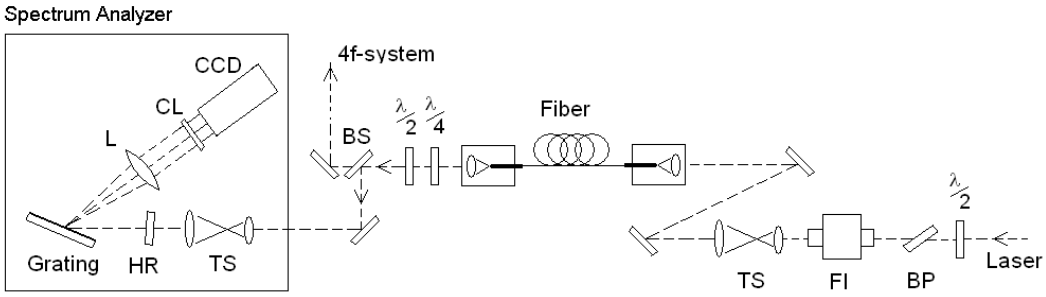

Figure 6: Scheme of the optical components and the fiber added to the laser oscillator for spectrum broadening. The spectrometer is also depicted.

the non-linear polarization P_{NL} of the source term depends on the cube of the field amplitude E

$$P_{NL} = \epsilon_0 \, \chi_{NL} \, |E|^2 \, E \tag{2}$$

where χ_{NL} is the non-linear susceptibility of the fiber mean. It is related to the non-linear n_2 refraction index of the total refraction index $n = n(\omega) + n_2 \, |E|^2$ by the relation

$$n_2 = \frac{\chi_{NL}}{\epsilon_o \, c \, n_0^2} \tag{3}$$

Eq. 1 after the SVEA (Slowly Varying Envelope Approximation) gives the equation governing the wave complex amplitude A

$$\frac{\partial A}{\partial z} = -\frac{1}{2} \, \alpha A - i \, \frac{1}{2} \, \beta \, \frac{\partial^2 A}{\partial^2 t} + i \, \frac{1}{L_{NL}} \, |A|^2 \, A \tag{4}$$

with β the propagation constant (in our fiber $\beta = 17 \, ps^2/km$) and α the the loss factor ($\alpha = 2.2 \, dB/km$). The first term of the equation is the loss term, the second term is the dispersion term (the longer the wavelength the faster the wave runs) and the third term governs the self-phase modulation. The quantity L_{NL}, called non-linear length, signs the starting of the non-linear action. Obviously, our goal requires $L_{NL} << L_{fiber}$. The relation

$$\frac{1}{L_{NL}} = \frac{\omega}{c} \, n_2 \, \frac{P}{\pi \, w_0^2} \tag{5}$$

gives the dependence of L_{NL} from the peak power P of the pulse. Here ω is the central frequency. The non-linear refraction index of our fiber resulted in our measurements $n_2 = 2.4 \cdot 10^{-20} \, m^2/W$, as from the tabulated fiber characteristics. The spectrum broadening $\Delta\omega_{out}$ from Eq. 4 comes out to be

$$\Delta\omega_{out} = \frac{L_{fiber}}{L_{nl}}\Delta\omega_{in} \propto P\, L_{fiber}\, \Delta\omega_{in} \propto P_M \cdot \frac{\Delta T}{\Delta\tau}\, L_{fiber} \cdot \frac{1}{\Delta\tau} \tag{6}$$

where P_M is the average power, ΔT is the the round trip time (in our cavity $10\ ns$) e $\Delta\tau$ the pulse temporal length.

In conclusion, once given the laser pulse power and the fiber characteristics the spectrum broadening depends on the fiber length. Eq. (4) has been solved numerically by the split stop Fourier method and the output spectrum obtained for our laser beam and optical fiber parameters is shown in Fig. 7. As expected when the output pulse of the laser is Gaussian, the smoothed phase function has a parabolic shape (that one of chirped pulses). Superimposed to the parabola there is a small fast oscillation of the phase. This oscillation is in correspondence of the power spectrum oscillation as shown by the figure. Frame b of Fig. 7 shows the measured power spectrum and the relative power spectrum calculated taking into consideration the resolution of the spectrometer. The limited resolution of the spectrometer is introduced into the calculations making the convolution of the theoretical spectrum of Frame a with a Gaussian curve of proper width (simulating the action of the spectrometer). The experimental result reproduces quite well the simulated one.

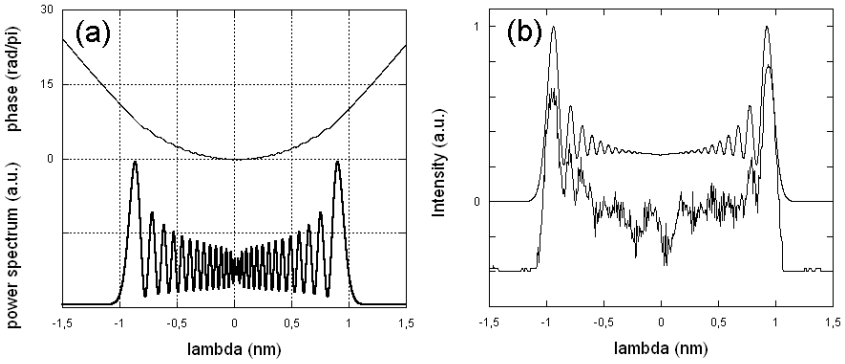

Figure 7: Frame a, simulated spectrum at the output of the optical fiber and the relative phase function. Frame b, the upper curve is again the simulated spectrum but convolved with a proper Gaussian curve, the power signal is the relative measured spectrum function.

A final observation is that the laser pulse length after the fiber is increased of about 10 % because of the dispersion.

3.1 The spectrum analyzer as powerful diagnostic tool

We have designed and built a spectrum analyzer tailored to the characteristics of our laser pulse, see Fig. 6: the grating of 1714 lines/mm is coupled to a lens of 400 mm focal length so to obtain a spatial dispersion of 0.68 nm/mm.

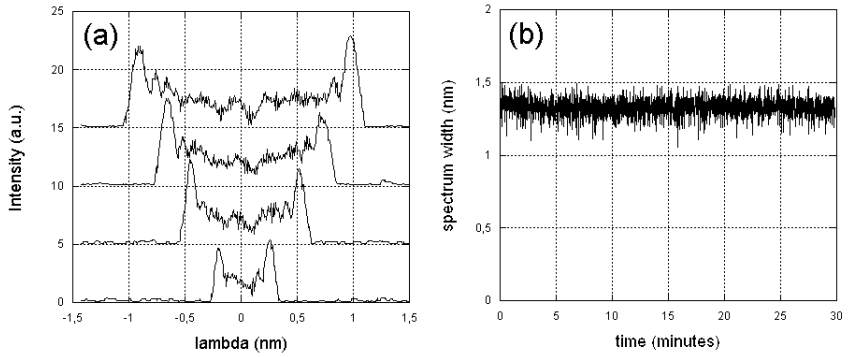

Figure 8: Frame a: set of measured spectra as function of the output average power, namely 100, 200, 300 and 400 mW respectively from bottom to top. Frame 2: jitter of the spectrum width in half an hour.

The linear enhancement of the spectrum bandwidth with the average laser power, as predicted by Eq.(6), is experimentally reproduced in Fig. 8, where the four spectra relative to 100-200-300-400 mW power are reported. In Frame b the variation of the spectrum which occurred within half an hour is depicted: it covers an interval amplitude of about 4 %.

Some technical observations are in order. We have observed a strict correspondence between the instability of the spectrum width and the average input power by the laser (resulted in the measurement of Fig. 8 of 2 % instability as expected from Eq. (6)).

Observing that $10\ \mu m$ variation of the cavity length leads to a quite different output waveform and in turn to a notable variation of the spectrum shape, we may use the spectrum analyzer as diagnostic tool of laser output signals. Hence, the power and the cavity tuning stability can be controlled via the spectrum stability. Once the relation between the laser pulse length at a given power level and the spectrum width is determined (via a cross check between analytical and experimental results), the spectrum width gives the pulse length. In this framework we could check that the pulse length corresponding to the spectrum width shown in Fig 6 was 78 ps.

We have discussed in detail the informations that are possible to extract from the spectrum measurement because this measurement is fast, in time and relatively much easier than the measurement of the temporal pulse length and its profile.

4 The LCP-SLM shaping system

The operational principle of the system, the computer program developed for the simulations with its performance and the configuration for an autoconsistent operation are

discussed. The main parameters are presented in Ref. [**?**].

The pulse shaping is a linear filtering process. In the time domain the filter action of the shaper is represented by an *impulse response function* $h(t)$, while in the frequency domain the filter action is represented by its Fourier transform $H(\omega)$. The output waveform $e_{out}(t)$ is the convolution of the input waveform $e_{in}(t)$ and the impulse response function h(t)

$$e_{out}(t) \; = \; h(t) * e_{in}(t) \tag{7}$$

In the frequency domain we may write

$$E_{out}(\omega) \; = \; H(\omega) \cdot E_{in}(\omega) \tag{8}$$

In general $H(\omega)$ will be a function of the type

$$H(\omega) = T(\omega) \cdot e^{-i\psi(\omega)} \tag{9}$$

Appropriate amplitude $T(\omega)$ and phase $\psi(\omega)$ modulations lead to any kind of output signal.

However, in problems where the demand is limited to the temporal intensity profile only, as is the case of rf-guns, a phase-only modulation can be applied. In fact, the time domain intensity (and amplitude) is specified but the temporal phases are free.

4.1 Operations of the shaping system

The optical components of a 4f-setup are two gratings and two lenses placed at the focal distances with a filter mask placed at the center focus plane, as shown in Fig. 9. The

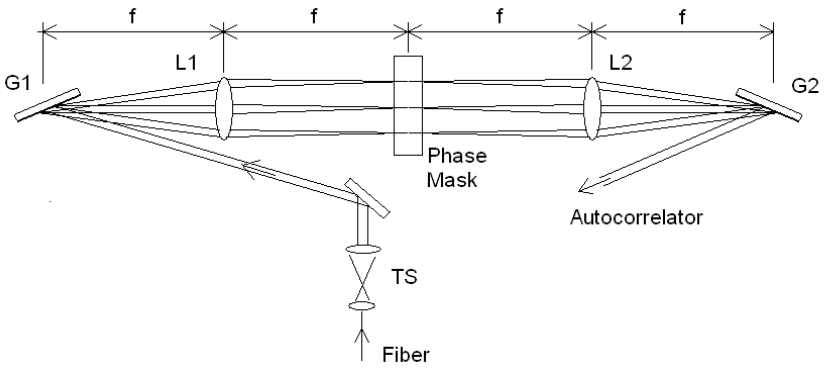

Figure 9: Scheme of the 4f-shaping system, top view. The light polarization lays on the plane of the figure (that is the plane of the optical table). The bold arrows indicate the state of the polarization

physical operations done by the device in the filtering process are: a) transformation of the input signal into a fan of spectral components by means of a grating, b) transformation of the components' fan into a comb of thin rays with a spot size w_0 by means of a lens, see Fig. 10, c) modulation, either in amplitude or in phase or in both, of the spectral components by a modulating mask, d) the back operations of transformation of the comb rays into a convergent beam by a second lens and e) re-combination of the components into a signal by a second grating. The output pulse profile is given by the Fourier transform of the pattern transferred by the mask onto the spectrum.

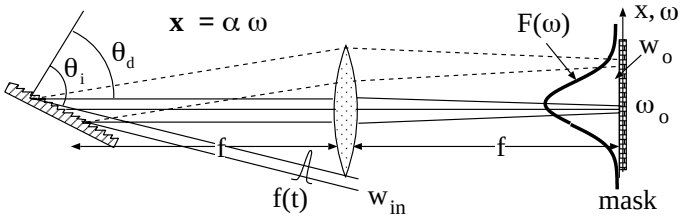

Figure 10: The input θ_i and diffracted θ_d angles by the grating of 4f-system. The mask and the grating are placed at the distance f from the lens. The Gaussian Fourier spectrum is depicted at the mask. The spectral components of the input light beam are separated by the grating and focused at the mask by a lens with a beam waist w_0.

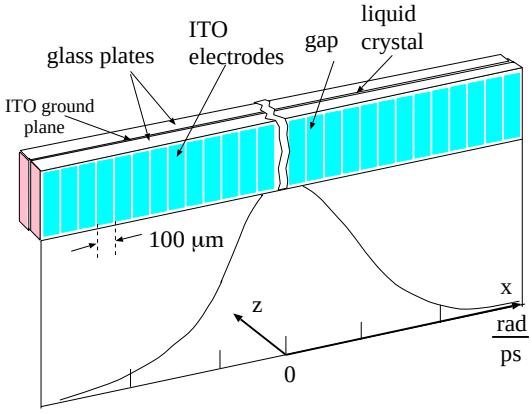

Figure 11: Schematic diagram of an electronically addressed LCP-SLM. A thin layer of nematic liquid crystal is sandwiched between two peaces of glass. The inside surface of each piece of glass is coated with a thin, transparent conducting film of indium tin oxide patterned as an array of pixels.

The mask of an LCP-SLM system is an array of pixels interleaved with small gaps, see Fig. 11. The chosen mask is the Jenoptik model SLM-S 640/12 mask (JENOPTIK Laser, Optik, System GmbH, Jena, Germany). The dimensions of the pixels and gaps are

respectively $97\ \mu m$ and $3\ \mu m$ wide and the number of pixels is 640.
The spectral dispersion follows, in first approximation, a linear law

$$x \simeq \alpha\omega \tag{10}$$

The frequency ω is referred to the central frequency ω_0 of the spectral domain spanned by the signal. The filter function $H(\omega)$ is related to the physical transmission function of the mask. We observe that the field just after the mask, calling $H_{SLM}(x)$ the physical transmittance of the mask, is given by

$$E_{out}(x,\omega) \sim H_{SLM}(x)\, e^{-\frac{(x-\alpha\omega)^2}{w_0^2}}\ E_{in}(\omega) \tag{11}$$

4.2 Configuration of the 4f-system

The configuration of the 4f-system is determined by the grating law and the equation of the beam waist w_0 at the mask pixel [**?**]

$$\lambda = d(sin\,\theta_i + sin\,\theta_d) \tag{12}$$

$$w_0 = \frac{cos\,\theta_i}{cos\,\theta_d} \cdot \frac{\lambda\, f}{\pi\, w_i} \tag{13}$$

In the above equations f is the focal length, λ is the wavelength, θ_d and θ_i are the diffracted and incident angles of the central frequency respectively (see Fig. 10) and w_i is the input beam waist at the grating.
The guidelines for the 4f-system configuration design are: (i) the spectral dispersion should be maximized so to exploit the maximum number of mask pixels and (ii) the beam waist at the pixel must be smaller-equal to the $100\ \mu m$ pixel dimension. Since the larger the dispersion the larger is the waist at the mask, the best trade-off must be found. We note also that the waist at the mask w_0 is inversely proportional to the waist w_i at the grating.
In our system we ended up to the following parameters: gratings with 1740 lines/mm, achromatic lenses of 50 cm focal length, 65^o degree input angle, $w_i = 2.3\ mm$ and $w_0 \leq 100\ \mu m$. In this configuration each nm of spectrum bandwidth covers 27 pixels of our mask.

4.3 The driving of the mask

The mask pattern configuration (filter function) is set by a computer through a serial gate. A voltage applied to the electrodes sandwiching the liquid crystal of a pixel drives the

crystal orientation. The voltage ranges in the interval 0-8 V with a step resolution of 12 bit (corresponding to 4096 possible voltage values). The principal axis of the crystal lays on the table plane x-z. This decides the polarization of the light coming from the grating for the highest efficiency.

The mask must be calibrated before starting the operation. This calibration operation is done setting the configuration of the 4f-system for the amplitude modulation. In this way we can build the curve T versus V. The amplitude modulator arranged in the Lab was made by a simple half-wave-plate set in front of the mask which rotates the polarization of 45^o and a polarizer set in the back of the mask at 90^o with respect the input polarization of the light. The transmittance T is given by

$$T = sin^2\left(\frac{\Delta\phi}{2}\right) \tag{14}$$

thus

$$\Delta\phi = \frac{2\pi\, d}{\lambda}\left[n_e(V) \,-\, n_0\right] \tag{15}$$

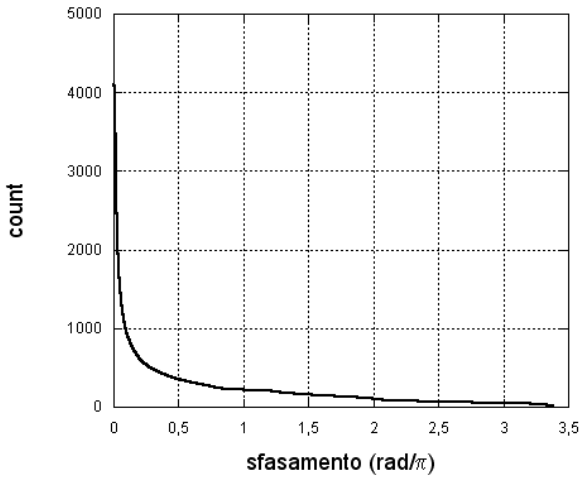

Figure 12: Curve of pixel voltage versus phase variation obtained in the calibration process.

The curve of the voltage, that is of the corresponding number, versus the phase modulation obtained with the apparatus is shown in Fig. 12. From the curve we get that the maximum de-phase on a spectral component (for our 1064 nm radiation) is higher than 2π but minor than 4π.
It is wise to select a zone of 2π variation and possibly linear. Therefore, we chose the

interval 0.5-2.5 rad/π. This means that we have 300 possible voltage values. We did the fit which transforms the voltage number into the phase modulation.

5 The autocorrelator for the pulse profile measurement

The common tool for the laser pulse profile measurement is a cross correlator. But this technique can be used only in conjunction with a laser pulse much narrower than the pulse to be diagnosed. Our laser does not allow to exploit that technique owing to its long output pulse. Therefore we have built an autocorrelator for the measurement. We are aware that there is not a strict correspondence between the autocorrelation pulse and the temporal pulse. However, the profile of the pulse can be derived from the autocorrelation output for a certain class of pulses as Gaussian, rectangular, multi-Gaussian, and others. Since these are the pulses of our interest, an autocorrelator can be positively considered. For completeness, we are developing a numerical code, as PICASO [7], capable of producing the temporal pulse profile from the autocorrelation plus spectrum signals. The schematic

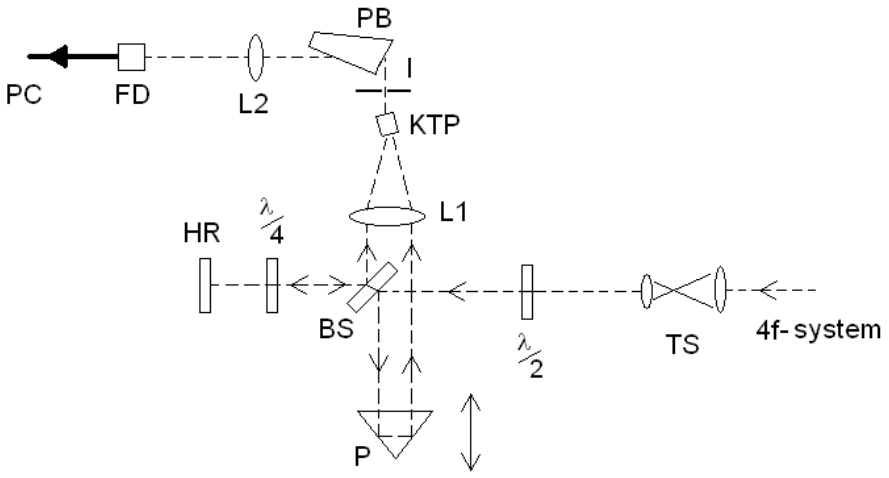

Figure 13: The design and the optical components of the autocorrelator are depicted.

of the built autocorrelator is shown in Fig. 13. The core of the autocorrelator is the KTP crystal where the two splitted input rays are focused so to generate the second harmonic through a phase-matching of the type 2 [8]. That crystal has a good non-linear coefficient and, more important, a relatively low sensitivity to alignment. The output signal is detected by a photodiode detector and sent to a computer after a analog-digital converter. For increasing the contrast noise-signal the IR component coming out together with the

up-converted signal must be suppressed as much as possible. To this aim after the doubling crystal are put an iris (the two green and IR beams have different directions) and a Pellin-Broca prism which is able to separate the two chromatic components.

6 A feedback arrangement of the shaping system for automatic operation

An analytical calculation of the response function H_{SLM} does not exist, it is found by a numerical calculation via an adaptive algorithm. The solution is implemented in the laser system by a proper setting of the shaping system. A computer, running the adaptive algorithm, can drive the system towards the right optical configuration of the mask.
The appropriate modulation (phase) function is calculated with an iterative procedure: the spectral patterned function is updated according to a Genetic stochastic optimization Algorithm (GA) [9,10]; a $cost - function$ C is calculated with the new signal obtained from the autocorrelator after the application at the mask of a fase function

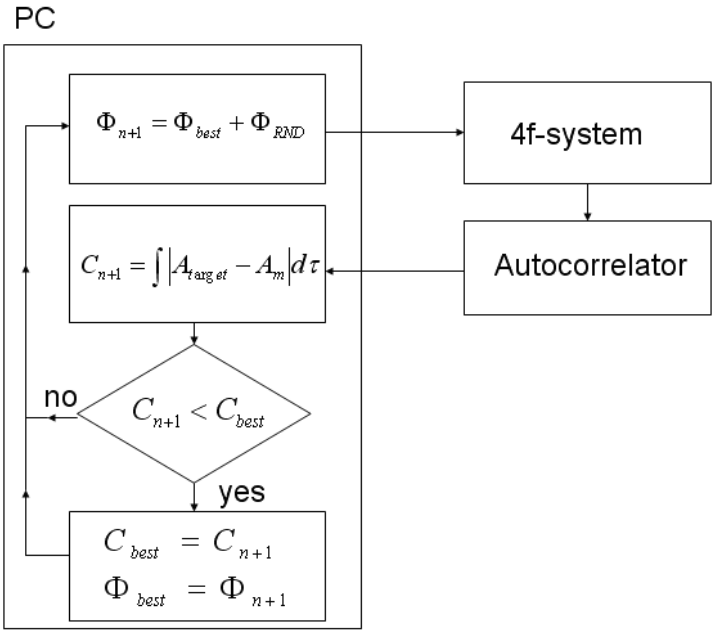

Figure 14: Flow chart of the numerical program for the simulation of the calculation of the phase function .

$$C = \int |A_{target}(\tau) - A_{measured}(\tau)| \, d\tau \quad ; \tag{16}$$

if the $cost - function$ results minor than the best $cost - function$ found in previous cycles, the updated spectral patterned function is accepted, otherwise it is rejected and a

new cycle starts with a fresh spectral pattern function. The iterations are stopped when the value of the $cost - function$ arrives to saturation. The final phase pattern is transferred to the mask. The complex spectral field $E(\omega)$ of the input pulse, that is its spectral amplitude $A(\omega)$ and phase $\Phi(\omega)$) and the temporal amplitude $E_{target}(t)$ of the target pulse are given as inputs. The calculation procedure is illustrated in Fig. 14. The initial trial phase vector Φ has all the phases at the pixels set at zero value and the value of the cost function is fixed very high.

We have followed two different numerical approaches. In one the phase function is written as a power expansion

$$\Phi_{rnd}(\omega) = a_{rnd}\,\omega^2 + b_{rnd}\,\omega^3 + c_{rnd}\,\omega^4 + \ldots \quad , \tag{17}$$

The adaptive algorithm searches for the appropriate phase filter function varying randomly the coefficients of the expansion and applying the iterative calculation up to the achievement of the best target profile [11]. In the second numerical approach the phase function is written as the sum of a function counter-fitting the main component of the curve representing the phase function of the imput signal and a spectral patterned randomly searched function $\delta\psi_{RND}(\omega)$

$$\Phi(\omega) = f(\omega) + \delta\psi_{RND}(\omega). \tag{18}$$

In each iteration a random phase change $\delta\psi_i$ is generated according to $\delta\psi_i = R$ where R is a random variable uniformly distributed in a definite interval. The index i refers to the i-th pixel. This second approach for our case of input pulse after the optical fiber, means that the function $f(\omega)$ is a parabola, that is the phase function will be

$$\Phi(\omega) = \frac{1}{2}\alpha_{rnd}\,\omega^2 + \delta\psi_{RND}(\omega). \tag{19}$$

The parabola counter-acts the parabolic phase generated by the self phase modulation effect within the optical fiber.

The first procedure does not give a positive result when the phase profile of the output pulse is complex. In fact, a phase function with fast oscillations requires many terms in the power development (17). The same consideration holds transform limited input pulses.

The succession of operations occurring in the system in each iteration are: a random variation of the phase function (by a computer), its application to the mask, re-orientation of the mask pixels (in about half a second) and a consequent generation of a new (varied) output pulse, measurement of the autocorrelation signal (the computer starts to acquire

from the autocorrelator the formed signal after 0.5 s from the releasing of the phase function), acquisition and renormalization (to unity) of its area, comparison of the signal with the target one via the cost-function and a new cycle starts.

7 Results and discussion

In this section we discuss the generation of four different waveforms shaped having as input pulse the chirped Gaussian-like pulse of about 110 ps provided by our laser system (oscillator and optical fiber). The system arrangement for the pulse modulation had to take into consideration a notable diffraction effect observed when the velocity of variation of the phase introduced for obtaining a new waveform was higher than a certain value. This effect is, therefore, treated in the next subsection in connection with the discussion of the first searched waveform. In our laser system we have to compare the autocorrelated target pulse with the autocorrelated output pulse from the 4f-system (instead of the direct temporal pulse).

7.1 Pulse compression to 2 ps length and the diffraction problem by the mask

The input pulse can be compressed setting a parabolic phase function to the mask which counteracts the phase modulation introduced by the fiber. The pulse, as shown in Fig. 15 Frame a, is compressed from the initial 110 ps to few ps. Frame b shows the phase function that the computer sent to the mask. The parabolic function is many-folded in order to maintain the phase variation among the pixels within the interval $-\pi \div +\pi$. The values of the phase function are converted in numbers that are sent to the mask.

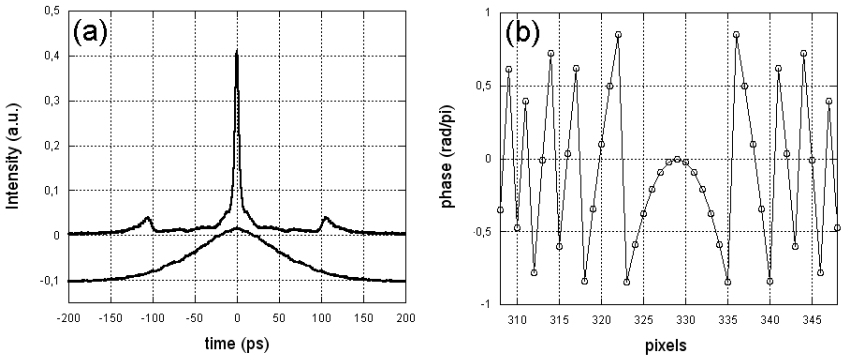

Figure 15: Frame a: the lower trace is the input 100 ps pulse and the upper trace is the 3 ps compressed pulse by the 4f-system; Frame b shows the phase function at the mask pixel.

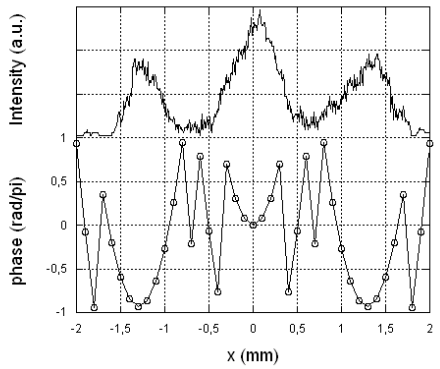

Figure 16: Intensity of the output signal obtained at a screen placed at 7 cm from the mask, upper trace, and the corresponding phase function, lower signal.

Remarkably, the output signal has two evident side pulses at a distance of about 100 ps from the main pulse. These pulses come out to be due to the fast slope of the parabolic phase curve (at the sides) necessary for the strong compression, which, in turn, means a large phase variation between two adjacent pixels. The effect is amplified by increasing the slope. We have observed on a screen, in fact, the appearance of two bright spots at the sides of the central spot starting from a certain slope. Looking at the position of the spots in relation to the phase curve, see Fig.16, we could see the correspondence between the bright spot and the smooth phase variation and, complementary, the dark place and the strong phase variation between the pixels.
Systematic observations on the intensity profile at the back of the mask lead to find the following empirical limit of the phase variation between two adjacent pixels

$$\frac{\Delta\phi_{max}}{\Delta\omega_{pixel}} = \frac{\pi/3}{\delta\omega_{pixel}} = \frac{\Delta\tau_{max}}{2}. \tag{20}$$

in order to avoid the diffraction action (remembering that the delay time between the frequency ω and the central frequency ω_0 is : $\tau(\omega) = \frac{\partial\phi(\omega)}{\partial\omega}$). This condition gives the maximum compression $\Delta\tau_{max}$ that can be obtained without meeting pulse deformation due to diffraction. In our system the maximum compressible pulse length comes out to be 40 ps. The check was done reducing the pulse length simply cutting the wings of the pulse at the mask site with an iris and then compressing that pulse. The result is shown in Fig. 17. The two 100 ps and 40 ps pulses after compression are compared in Frame b: the second pulse is much more neat compared with the other. This mask behavior limits the shaping possibility because only a limited spectrum bandwidth is accepted with a pulse of that length. Therefore, the diffraction effect of the mask limits the rise time of a target

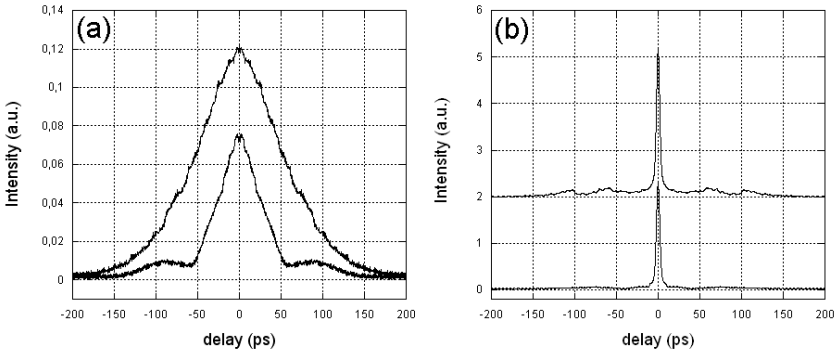

Figure 17: Frame a: the upper and the lower autocorrelation traces of the input pulse respectively without the iris in front of the mask (the laser pulse) and with the iris. Frame b: the two corresponding pulses compressed by the shaping system. The compressed pulse obtained with the iris insertion is much more neat.

rectangular profile.

7.2 A rectangular profile

The autocorrelation signal of a rectangular pulse has a triangular profile. The target pulse to be built was a rectangular one of 10 ps length. In this case the power expansion procedure requires only the second and the forth terms because of the parabolic profile of our input phase function. In Fig. 18 the two autocorrelation pulses, the target and the experimental one, are reported. In Frame b the cost function behavior with the number of iterations is reported. The two target and experimental signals overlap quite well, and the result is obtained in only 30 iterations. The rise time is about 3 ps because of the relatively narrow spectral bandwidth.
We would remark the good result with a relatively fast convergence in spite of the particular form of the input signal. In the most common case of a transform limited pulse (obtained for instance from a Ti:Sa laser) the number of necessary terms for obtaining a rectangular pulse would be not more than eight. Fig. 19 shows the result obtained applying the second procedure: the two signals do not match as in the previous operation and the number of iterations required is about a factor three higher. This is explained by the different calculation procedure: in the previous procedure only two coefficients were varied randomly, while in the second procedure all the phases of a patterned function relative to the array of pixels had to vary randomly. Moreover, the very good fit obtained in the first procedure was due to the peculiar spectral function after the interaction within the fiber.

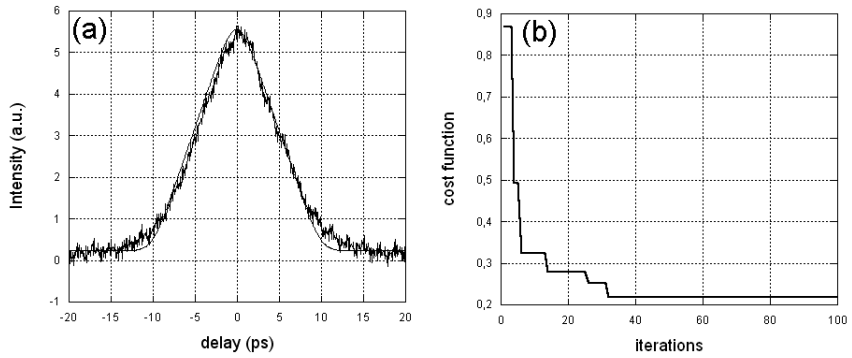

Figure 18: Frame a: the two target and measured autocorrelation signals of the rectangular pulse; Frame b: the number of iterations required for obtaining the final signal.

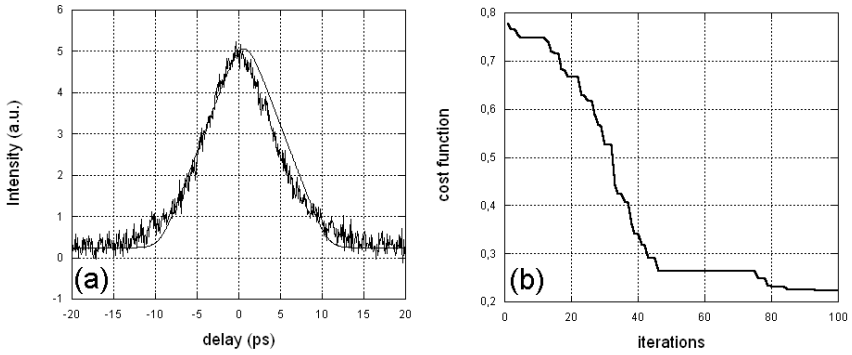

Figure 19: As previous Fig. 18 but the numerical simulation followed the second procedure. Frame a: the two target and measured autocorrelation signals of the rectangular pulse; Frame b: the number of iterations required for obtaining the final signal.

7.3 A double-pulse profile

The generation of a pair of pulses (pump-probe pulses) is another result interesting for several applications. The target pulse is a pair of pulses of 4 ps width and 12 ps interdistance. The result is shown in Fig.20. Again the output pulse reproduces quite well the target pulse. The proper procedure for this case was the second one and the number of iterations was higher than the previous case. Two remarks are worth doing: one is that the initial value of the cost-function was set at a much lower level than in the previous cases and the second one is that there is a proper temporal window for the integral of the cost-function. The initial low value of the cost-function is due to the relatively large width of the autocorrelation target pulse (not far from that of the input pulse). The temporal interval of integration cannot be too large because the integral would be affected by the

numeral noise and would lead to a low value of the cost-function. It cannot be too short, on the other side, because the information on the shape of the whole pulse would be lost.

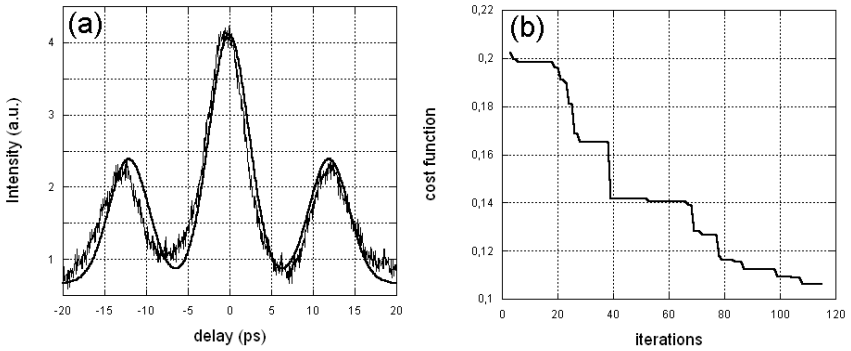

Figure 20: Frame a: the two target and measured autocorrelation signals of a double pulse profiles; Frame b: the number of iterations required for obtaining the final signal.

7.4 A multi-pulse profile

The spectral filtering technique can be used for generating high-repetition-rate pulse trains. A pulse shape is the Fourier transform of the pattern transferred by the spatial filter onto the spectrum [12]. In our approach we use a spectral phase filtering: the phase response of the mask (filter) varies periodically with frequency, see Fig. 21. In this way the spectral bandwidth is divided in N sub-bandwidths whose distance in frequency is ΔF. Each radiation sub-bandwidth is conveyed into the relative pixel sub-array and will apply the same phase modulation. The repetition rate of the train is the frequency periodicity ΔF.

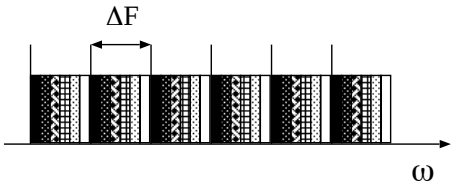

Figure 21: Generation of a pulse train by a phase spectral filtering. The various shaded rectangles denote the pixels with different phases.

The output intensity profile $I(t)$ is related to the input waveform $E(\omega)$ as

$$I(t) = \left(\frac{1}{2\pi}\right)^2 \int e^{i\,\omega\,t} d\omega \int E^*(\omega')\, E(\omega' - \omega)\, d\omega' \tag{21}$$

The intensity is the Fourier transform of the autocorrelation of the filtered spectrum. To obtain a set of pulses under a smooth envelope by using a phase filter, we must make a phase response with an autocorrelation that consists of a train of spectral peaks. Various pseudorandom phase sequences can provide this sequence.
The pixel were grouped in bunches of 5. The phase mask consisted of the repetition of the sequence [10010] where the logic 1 corresponded to $\Delta\phi = 0.7\pi$. The phase mask is sufficiently wide to pass the entire input bandwidth; consequently, the pulses in the shaped train are as short as the input pulses, $\simeq 3ps$ FWHM. Figure 22 shows the auto-correlation measurement of of the pulse train.

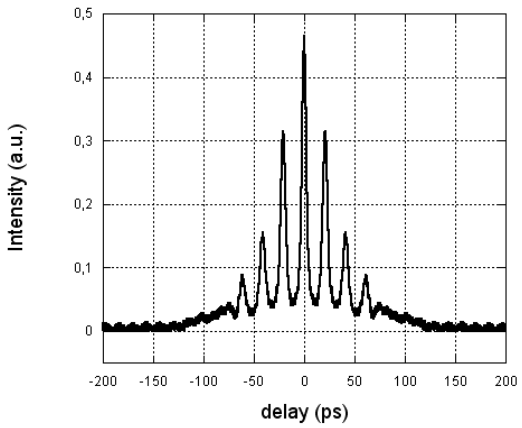

Figure 22: Auto-correlation measurement of the pulse train produced by phase periodical filtering.

8 Conclusions

The relatively low-cost medium technology laser system built in the LAB has demonstrated to be a good light source for research and development of shaping techniques. With it we tested the generation of many pulse profiles and developed the relevant computer programs for driving the shaping system as well as we could test the arrangements for optimized operations.

The up-grading of the laser source for the generation of dozen picosecond pulses is under progress. The goal is pursued through the implementation in the oscillator of a SESAM [13] (semiconductor saturable absorber). The foreseen pulse length of about 40 ps, instead of the to-day 80 ps, would allow to increase of, at least, a factor four the spectral bandwidth of the pulse with respect to the present bandwidth of 3 nm. The new

feature of the light source will allow to do tests on picosecond rise times of rectangular pulses. In addition, the cross correlation diagnostic would become feasible.

Acknowledgments

We must thank F. Castelli for fruitful discussions and valuable criticisms. The work is partly supported by Ministero Istruzione Universita' Ricerca, *Progetti Strategici*, DD 1834, Dec,4,2002 and European Contract RII3-CT-PHI506395CARE.

References

[1] SPARC "Conceptual design of a high-brightness linac for soft X-ray SASE FEL source," EPAC 2002 (La Villette, Paris) 5 June 2002.

[2] M. Cornacchia et al., "Linac coherent light source (LCLS) design study report" (Stanford University-University of California) Report No. SLAC-R-521/UC-414, revised 1998.

[3] F. Richard et al, "TESLA, the superconducting electron-positron linear collider with an integrated X-ray laser laboratory, technical design report," Desy Report No. DESY2001-011, ISBN 3-935702-00-0, 2001

[4] J. Yang, F. Sakai, T. Yanagida, M. Yorozu, Y. Okada, K. Takasago, A. Endo, A. Yada, and M. Washio, J. Appl. Phys. **92,** 1608–1612 (2002).

[5] A. M. Weiner, Rev. Sci. Instrum., **71,** 1929-1960 (2000).

[6] P. Tournois, Opt. Commun. **140,** 245–249 (1997).

[7] J.W. Nicholson, J. Jasapara, W. Rudolph, F.G. Omenetto and A.J. Taylor, Opt. Lett. **24**, 1774-1776 (1999).

[8] W. Koechner, *Solid-State Laser Engineering* Springer.

[9] D. Meshulach, D. Yelin, and Y. Silberberg, Opt. Commun. **138,** 345–348 (1997).

[10] D. Meshulach, D. Yelin, Y. Silberberg, J. Opt. Soc. Am. B **155,** 1615–1619 (1998).

[11] S. Cialdi, I. Boscolo and A. Flacco, J. Opt. Soc. Am. **21**, 1693-1698 (2004).

[12] A.M. Weiner and D.E. Leaird, Opt. Lett. **15**, 51-53 (1990).

[13] C. Honninger, R. Paschotta, F. Mourier-Genoud, M. Moser and U. Keller, J. Opt. Soc. Am. B/**16**, 46-56 (1999).